INTERFACE

royalsocietypublishing.org/journal/rsif

Research

Cite this article: Quirk K, Boster KAS, Tithof J, Kelley DH. 2024 A brain-wide solute transport model of the glymphatic system. *J. R. Soc. Interface* **21**: 20240369.
https://doi.org/10.1098/rsif.2024.0369

Received: 29 May 2024
Accepted: 4 September 2024

Subject Category:
Life Sciences–Mathematics interface

Subject Areas:
computational biology, biomechanics, biomedical engineering

Keywords:
sensitivity analysis, glymphatic system, reduced-order modelling, solute transport, perivascular spaces, computational modelling

Author for correspondence:
Douglas H. Kelley
e-mail: d.h.kelley@rochester.edu

A brain-wide solute transport model of the glymphatic system

Keelin Quirk[1], Kimberly A. S. Boster[1], Jeffrey Tithof[2] and Douglas H. Kelley[1]

[1]Department of Mechanical Engineering, University of Rochester, Rochester, NY 14627, USA
[2]Department of Mechanical Engineering, University of Minnesota, Minneapolis, MN 55455, USA

KQ, 0009-0002-1078-9028; KASB, 0000-0001-5178-128X; JT, 0000-0003-2083-0901; DHK, 0000-0001-9658-2954

Brain waste is largely cleared via diffusion and advection in cerebrospinal fluid (CSF). CSF flows through a pathway referred to as the glymphatic system, which is also being targeted for delivering drugs to the brain. Despite the importance of solute transport, no brain-wide models for predicting clearance and delivery through perivascular pathways and adjacent parenchyma existed. We devised such a model by upgrading an existing model of CSF flow in the mouse brain to additionally solve advection–diffusion equations, thereby estimating solute transport. We simulated steady-state transport of 3 kDa dextran injected proximal to the perivascular space (PVS) of the middle cerebral artery, mimicking *in vivo* experiments. We performed a sensitivity analysis of 11 biological properties of PVSs and brain parenchyma by repeatedly simulating solute transport with varying parameter values. Parameter combinations that led to a large total pressure gradient, poor CSF perfusion or a steep solute gradient were deemed unrealistic. Solute concentrations in parenchyma were most sensitive to changes in pial PVS size, as this parameter linearly affects volume flow rates. We also found that realistic transport requires both highly permeable penetrating PVSs and high-resistance parenchyma. This study highlights the potential of brain-wide models to provide insights into solute transport processes.

1. Introduction

The human brain comprises just 2% of the body's mass but is responsible for approximately 20% of the body's energy expenditure, making it a prodigious producer of metabolic waste. Since brain tissue lacks lymphatic vessels, which aid in metabolic waste clearance elsewhere in the body [1,2], it has long been speculated that flow of cerebrospinal fluid (CSF) may aid in the brain clearance [3,4]. The idea of a glymphatic system, which serves the function of a lymphatic system in the brain and is controlled by glial cells, was proposed when bulk CSF flow was first observed to couple with vascular pulsations [5,6].

In the decade since, additional experiments have confirmed that CSF passes through perivascular spaces (PVSs), which are annular channels around arteries and veins, flowing in the same direction as blood [7–11]. While mice and rats have been studied most extensively, similar CSF flows are seen in pigs [12] and alligators [13]. Human CSF flow has been thoroughly investigated on the brain-wide scale [14–16]. However, the spatial and temporal resolution of non-invasive techniques employed in human studies is much lower than that achievable in invasive animal experiments, making quantification of fluid motion in PVSs challenging [17].

To complement and direct future experimental measurements, several notable brain-wide models of glymphatic fluid motion have been developed. Analytical models of fluid transport of individual PVSs have been used

THE ROYAL SOCIETY PUBLISHING

to explore mechanisms driving flow [18,19]. The first brain-wide model of perivascular fluid flow [20] used a branching tree model of PVSs. This model estimated the hydraulic resistance of branching pathways and was used to ask which conditions could reproduce previously measured flow rates without the total pressure drop exceeding a theoretical limit. Another brain-wide model [21] used the model geometry shown in figure 1, accounting for interconnected loops present in the pial (surface) vasculature [23]. A global pressure drop was selected to reproduce previously measured velocities. All such models suffer from considerable uncertainty in some of the parameters needed to estimate hydraulic resistances. A sensitivity analysis subsequently performed on the model of Tithof *et al*. [21] indicated that the total conductance of the model was highly dependent on the permeability of penetrating PVSs, suggesting the need for more accurate measurements of that quantity [24]. Models such as these are helpful in guiding *in vivo* experiments.

While brain-wide fluid transport models have offered useful insight into possible mechanisms that drive flow, no brain-wide models of solute transport through PVSs as well as brain tissue have yet been developed. Several previous solute transport models have considered solute motion through porous brain tissue alone [25–27], PVSs alone [28], or through the entire brain [29]. Additional models have used compartments to represent possible different fluid pathways rather than accounting for PVS geometry explicitly [30,31]. Studies of solute transport are essential because neurodegenerative disorders are often caused by accumulation of toxic solutes [32–34]. Solutes are removed more efficiently during sleep, when PVSs expand [14] and brain tissue becomes more permeable [35]. Further research on solute transport through glymphatic pathways and brain tissue is needed to understand the relationship between glymphatic clearance, sleep and the development of neurodegenerative diseases.

In this study, we expanded the hydraulic network model described by Tithof *et al.* [21] (figure 1*a–c*) to solve for steady-state solute transport in the PVSs around arteries and the adjacent parenchyma (figure 1*d,g*). We calculated solute transport throughout the network for simulations in which the average fluid velocity in pial PVSs matched experimental measurements [7,21,24]. First, the hydraulic network model was run with the pressure drop for which the mean velocity in the first three generations of pial segments was 18.7 $\mu m\, s^{-1}$ (figure 1*d*), to match measurements of CSF speed in pial spaces along the middle cerebral artery in mice [7]. Then, the steady-state, one-dimensional (1D) advection–diffusion equation was solved analytically in each network segment. We then varied 11 geometrical parameters of the model, repeatedly simulating, to determine how solute transport rate, total concentration gradient and parenchymal concentration varied with the geometry, using an approach like that of Boster *et al.* [24]. We also explored which parameters are important for realistic model behaviour, as well as for sleep–wake variations of glymphatic influx and solute transport. These sensitivity analysis results can inform future *in vivo* experiments, as they highlight the parameters of greatest impact for estimating solute transport.

2. Methods

2.1. Solute transport equations in perivascular spaces and parenchyma

The network of PVSs in this model represents the middle cerebral artery and the penetrating arteries that descend from it, as introduced by Tithof *et al*. [21]. We simulated a dye injection, for which there is a constant high concentration of solute at the inlet, arbitrarily set to a concentration value of 100. We then assumed solute clearance along perivenous efflux routes to be fast relative to the time scale for dye injection experiments, which generally are analysed 30 min after injection [22]. Thus, we fix a zero concentration condition at all pericapillary and parenchymal outlets. This assumption of fast solute clearance is common in previously published models of solute transport through the parenchyma [25,36].

We approximated PVSs as 1D because they are long and thin and transport solutes primarily along their lengths. We modelled the PVS network as a collection of connected segments. Steady-state solute concentration in a 1D segment was governed by

$$u_i \frac{\partial c_i}{\partial z} = D_i \frac{\partial^2 c_i}{\partial z^2}, \tag{2.1}$$

where i is the segment number, c_i is the concentration in that segment, u_i is the average velocity, z is the position along the segment and D_i is the solute diffusion coefficient. This ordinary differential equation can be solved by

$$c_i = \frac{A_i D_i}{u_i} e^{u_i z / D_i} + B_i, \tag{2.2}$$

where A_i and B_i are constants determined by boundary conditions.

The existing brain-wide fluid model allowed for the possibility that capillary PVSs provide a fluid pathway linking arterial and venous PVSs, but when run, the model almost always predicted that little fluid flowed along capillary PVSs. Instead, the dominant pathway in simulations involved fluid flow through the walls of the penetrating PVSs and then outward through the brain parenchyma [21]. There, it passes through extracellular space, so we modelled the parenchyma as a porous medium, with the approximations that arterial PVSs are long and straight, and that the surrounding parenchyma is axially symmetric around the PVS. The Darcy equation that governs the flow is therefore 1D and has solution $\boldsymbol{u} = q\hat{r}(2\pi r)^{-1}$, where $\boldsymbol{u}$ is the (superficial) fluid velocity, q is the volume flow rate per axial length of PVS, $\hat{r}$ is the unit vector in the cylindrical radial direction and r is the cylindrical radius. Again using the same symmetry assumptions, the solute concentration in segment i of the parenchyma is governed by

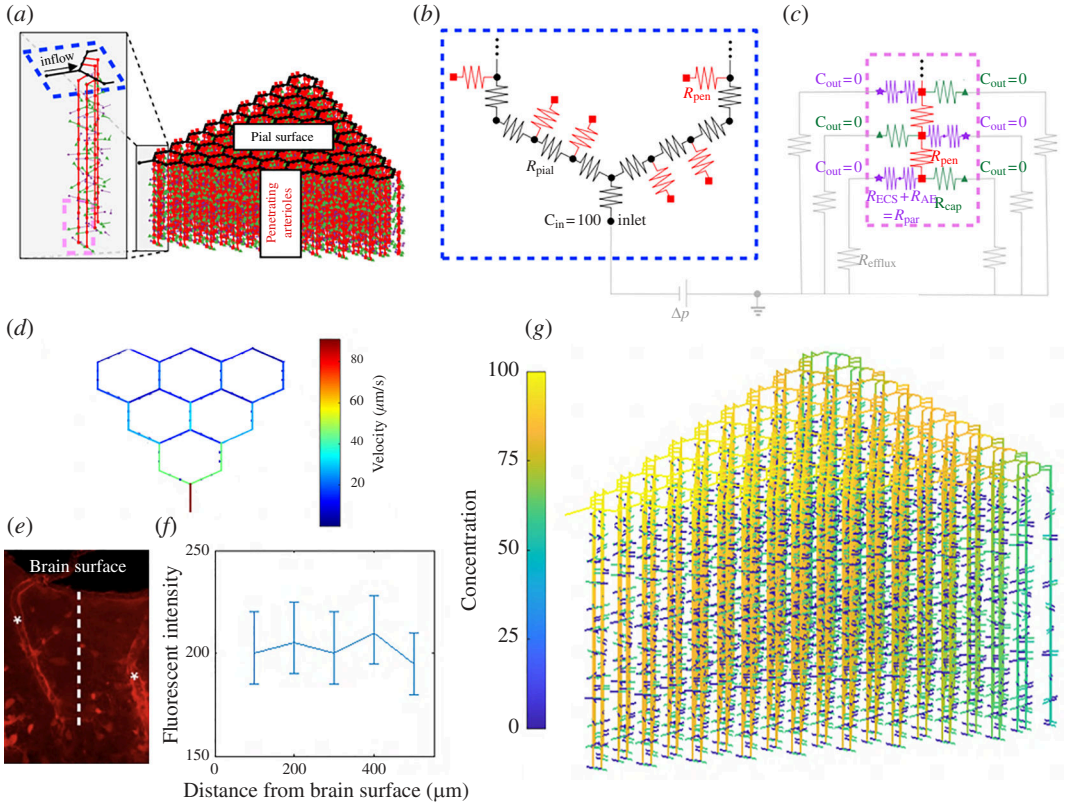

Figure 1. (*a–c*) The modelled perivascular geometry, with colours indicating different vessel types, adapted from [21]. Blue and pink dashed lines surround the model regions that are enlarged in (*b*,*c*). (*b*) Hydraulic resistances model pial PVSs (black), penetrating PVSs (red) and all other segments. (*c*) Capillary PVSs (green) and parenchymal segments (purple) branch from each penetrating PVS. (*d*) The velocities in the first three generations of pial PVSs are used to calculate the appropriate pressure drop. For all simulations, the mean velocity in these pial segments is set as 18.7 μm s^{-1} to match corresponding velocity measurements along the middle cerebral artery in mice [7]. (*e*) *In vivo* measurements of 3 kDa dextran concentration in a mouse hypothalamus, 30 min after intracisternal injection, adapted from [22]. Penetrating PVSs are identified with asterisks. (*f*) The fluorescence measured along the penetrating PVSs, as indicated by stars in (*e*), adapted from [22]. The error bars indicate the standard deviation of measurements from $n = 4$ mice [22]. (*g*) The average concentration in each segment, predicted by an example simulation. The concentration was held at 100 at the inlet and 0 at the outlets.

$$\frac{q}{2\pi r}\frac{\partial c_i}{\partial r} = D_i\left(\frac{\partial^2 c_i}{\partial r^2} + \frac{1}{r}\frac{\partial c_i}{\partial r}\right). \tag{2.3}$$

The solution is

$$c_i = (r/R)^{q_i/(2\pi D_i)}(X_i - Y_i)Y_i, \tag{2.4}$$

where X_i and Y_i are again unknown coefficients of integration and R is the radius of the parenchymal segment.

To determine the two unknown coefficients in every segment, we set the concentrations of the network inlet and outlets as boundary conditions and solved the resulting system of equations. Where segments met, concentration was required to be continuous and solute influx was required to equal solute efflux. The solute flux in a PVS is given by

$$J_i = S_i\left(c_i u_i - D_i\frac{\mathrm{d}c_i}{\mathrm{d}z}\right), \tag{2.5}$$

where S_i is the area through which the solute passes. Using the expression for c_i given by equation (2.2), the solute flux in a PVS becomes

$$J_i = S_i B_i u_i. \tag{2.6}$$

The solute flux in a parenchymal segment is given by

$$J_i = 2\pi r h\left(c_i u_i - D_i\frac{\mathrm{d}c_i}{\mathrm{d}r}\right), \tag{2.7}$$

where h is the axial length of the parenchymal segment. Using the expression for c_i given by equation (2.4), the solute flux in a parenchymal segment becomes

$$J_i = \pi r h Y_i u_i. \tag{2.8}$$

Thus, at a bifurcation, we require that the total solute flux entering the bifurcation, J_{in}, equals the total solute flux exiting the bifurcation, J_{out}. At pial bifurcations, some solute efflux is due to CSF escaping into the subarachnoid space, as set by E_{pial}, the fraction of fluid that escapes [24].

2.2. Numerical implementation

Equations (2.6) and (2.8) together form a system of linear equations, which we solved in matrix form in MATLAB. The unknown coefficients were placed in a column matrix called A, and inhomogeneous terms, namely the applied concentration at the inlet, were placed in a column matrix called R. The known variables multiplying each unknown coefficient were placed in a sparse square matrix L. The matrix equation $L \times \vec{A} = \vec{R}$ then represented the entire system.

We determined the matrix of unknown coefficients using the generalized minimum residual method in MATLAB, which iteratively solves the linear equation $A = \text{inv}(L) \times R$. Variable-precision arithmetic was necessary for segments with a large Péclet number because their outlet concentrations depend on e^{Pe}. The Péclet number, which is the ratio of solute advection to diffusion, is defined as $Pe = ul/D$, where u is the velocity, l is the length of each segment and D is the diffusion coefficient. The condition number of the matrix L was large in most simulations. A typical simulation result, which shows the average steady-state concentration, appears in figure 1*g*.

To provide enough known values to solve this system of equations, it is necessary to prescribe values for the concentration at all inlet and outlet points. The units of concentration in this model are arbitrary, with the inlet concentration assigned a value of 100, while the outlet concentrations are assigned a value of 0.

2.3. Diffusion of dextran through open and porous perivascular spaces

Modelling solute transport requires first choosing a solute of interest. Many *in vivo* experiments, including that of Mestre *et al*. [22], used Texas Red-conjugated dextran with molecular weight 3 kDa. The diffusion coefficients of dextran are well studied. In a dilute agarose solution, the free diffusion coefficient was found to be $2.33 \times 10^{-10}\,\text{m}^2\,\text{s}^{-1}$, and in a cortical slice, the effective diffusion coefficient was found to be $8.11 \times 10^{-11}\,\text{m}^2\,\text{s}^{-1}$ [37]. We used these values as diffusion coefficients in the pial PVSs and the parenchyma, respectively.

The effective diffusion coefficient is a function of the tortuosity of the space λ: $D_{\text{eff}} = D/\lambda^2$. While measurements of the tortuosity and porosity of the penetrating PVSs and capillary PVSs are unknown, permeability can be estimated from tortuosity using the Kozeny–Carman equation [38]:

$$\kappa = \frac{\alpha^3}{\lambda S^2(1-\alpha^2)}, \tag{2.9}$$

where κ is the permeability, α is the porosity, λ is the tortuosity and S is the surface area. Experimental validation is needed to confirm the tortuosity of the penetrating and capillary spaces, but as an initial approximation, the effective diffusivity was assumed to vary as a function of permeability.

In a given simulation, the effective diffusion coefficient for a porous PVS was scaled between the diffusion coefficient for an open space and the diffusion coefficient in the parenchyma. Because the range of permeabilities is several orders of magnitude, the scaling is based on the log of the permeabilities. The maximum permeability for penetrating and capillary spaces in table 1 corresponds to the equivalent permeability of an open PVS [21], in which case the effective diffusivity is the free diffusion coefficient D. Since the measurement of the diffusion coefficient in brain tissue was not associated with a specific value of permeability or tortuosity [37], this was treated as a minimum value for all diffusion in brain tissue or PVSs. Thus, in the case where a PVS is less permeable than the parenchyma, the low-permeability PVS and parenchyma both have a diffusivity of $8.11 \times 10^{-11}\,\text{m}^2\,\text{s}^{-1}$.

2.4. Quantifying global concentration gradients

It is useful to quantify global variation of concentration. To do so, we used the Dirichlet energy $\mathcal{E}(c)$ on the network's line graph, defined as

$$\mathcal{E}(c) = \vec{c}^{\,T}\mathbf{L}_{\mathbf{L}}\vec{c}, \tag{2.10}$$

where $\vec{c}$ is an array with a length equal to the number of segments in the network containing the average concentration in each segment and $\mathbf{L}_{\mathbf{L}}$ is the Laplacian of the line graph, with indices of −1 indicating which segments are connected. Thus, $\mathcal{E}(c)$ is the sum of the squared differences between all connecting segments. Large values indicate greater variation and often correspond to high concentration in the pial and penetrating spaces with low concentration in the capillary and parenchymal spaces.

2.5. Model parameters

In total, the hydraulic network model requires 23 material and geometrical parameters as inputs, and the solute transport model requires two additional parameters describing the diffusion in the pial PVS and parenchyma, since the diffusion coefficient in the penetrating and capillary PVS scales with the permeability. As the model includes geometrical and material parameters that are difficult to measure experimentally, there is considerable uncertainty in some of those parameters. Table 1 lists 11 parameters varied for this sensitivity analysis. These are the same parameters varied by [24]. The majority of these parameters

Table 1. Parameter range for the sensitivity analysis on solute transport. Ranges are the same as those used for a sensitivity analysis on model conductance [24], with the exception of capillary area ratio. The upper bound of capillary area ratio has been increased to allow for low-resistance capillary PVSs.

	parameter		lower bound	upper bound
pial	fraction pial efflux	E_{pial}	0 [39]	0.8 [39]
	pial PVS area ratio	Γ_{pial}	0.5 [7,40]	2 [7,40]
penetrating	penetrating PVS area ratio	Γ_{pen}	0.5 [7]	2 [7]
	penetrating PVS permeability (m^2)	κ_{pen}	4.50×10^{-15} [41]	3.71×10^{-12} [42]
capillary	capillary PVS permeability (m^2)	κ_{cap}	2.25×10^{-18} [43]	4.66×10^{-14} [44]
	capillary area ratio	Γ_{cap}	0.07 [45]	2 [46]
	capillary effective length (m)	L_{cap}	5.00×10^{-5} [21]	4.00×10^{-4} [21]
	capillary radius (m)	r_{cap}	1.50×10^{-6} [47]	4.5×10^{-6} [47]
parenchymal	parenchyma permeability (m^2)	κ_{par}	1.2×10^{-17} [42]	4.5×10^{-14} [36]
	endfoot wall thickness (m)	T	2.00×10^{-7} [48]	1.00×10^{-6} [48]
	endfoot cavity fraction	F_c	0.003 [48]	0.37 [49]

(E_{pial}, κ_{pen}, κ_{cap}, L_{cap}, r_{cap}, κ_{par}, T and F_c) have not been carefully measured experimentally, leading to a large range of measured or estimated values. Γ_{pial} and Γ_{pen} were included because PVS area can vary significantly with location in the brain [40]. The upper bound of the capillary area ratio was set higher than in Boster *et al*. [24] because recent patient-specific models of solute transport in human brains found that low resistance could induce pericapillary flow [46], a possibility we wanted to consider. Other parameter ranges were left unchanged from Boster *et al*. [24].

The simulations maintained fixed values for several model parameters throughout the sensitivity analysis. One such parameter was the number of pial PVSs, which follow a branching hexagonal model originally proposed by Blinder *et al*. [50]. This model comprises 45 hexagonal pial units extending across nine generations, with 324 penetrating arterioles descending from the pial vasculature. The number of arterioles closely aligns with measurements near the middle cerebral artery [51]. Another fixed parameter, the number of pericapillary branches associated with each penetrating arteriole, was set at 11, consistent with measurements by [23]. Thus, the number and location of PVSs were consistent across simulations. Additionally, the artery diameters for pial and penetrating arteries are variable parameters in the model, which we opted to fix in the sensitivity analysis. Given the area ratios for both types of PVSs were varied in our analysis, independent adjustment of inner diameters was unnecessary. Lastly, the shapes of PVSs, quantified by Tithof *et al*. [52], remained the same in each simulation.

Varying the values of the 11 uncertain parameters across their ranges and using Latin hypercube sampling, we solved the model for 1000 different combinations of parameter values. Any parameter whose range spanned less than one order of magnitude was sampled uniformly, while any parameter with greater span was sampled with a log-uniform distribution.

In each simulation, we applied a global pressure drop sufficient to drive an 18.7 $\mu m\, s^{-1}$ flow along the first three pial PVS generations, to match *in vivo* measurements in mice [7]. This is different from the pressure drop applied previously, which was chosen to drive a flow with mean velocity 18.7 $\mu m\, s^{-1}$ along all nine pial generations [21,24]. Accordingly, velocities were typically lower in our simulations than in previous work.

2.6. Sleep–wake simulations

Glymphatic flows are more substantial during sleep [35,53], so we also simulated sleep and wakefulness. In all simulations in the sensitivity analysis, the velocities in the pial PVSs were set to match velocities observed in mice anaesthetized with Ketamine-xylazine [7]. Solute transport in mice under Ketamine-xylazine is very similar to solute transport in naturally sleeping mice [35], so these simulations are also representative of solute transport following a period of natural sleep.

Following the procedure of [21], we modelled the awake brain by decreasing the permeability of the parenchyma by a factor of 5.5 but keeping all other parameters, including the applied pressure drop, the same. The total resistance in the parenchyma depends both on the resistance of the extracellular spaces in parenchymal tissue R_{ECS}, as well as on the resistance of the astrocyte endfoot gaps R_{AE}. This is shown in figure 1*c*, where these two resistances are in series. Simulating wakefulness by altering the parenchymal permeability in this way linearly increases R_{ECS} by a factor of 5.5, while R_{AE} remains unchanged.

2.7. Criteria for realistic transport

While boundary conditions were chosen to produce appropriate flow speeds in the pial PVSs, additional information about brain fluid motion can also be applied to check if model predictions are consistent with real glymphatic transport. Though the global pressure drop across a murine glymphatic system has never been measured, it is expected to be less than 1 mmHg. Additionally, since good perfusion would be necessary for effective glymphatic transport, it is expected that at least 50% of the

fluid efflux from PVSs to parenchyma occurs distal to the first of the 11 bifurcations along the penetrating PVSs. This bifurcation occurs about 90 µm below the pial surface, and the fraction of fluid that exits the perivascular space at that first bifurcation is defined as ϕ_{90}. Simulations that failed to meet either of these expectations were deemed unrealistic, as in a prior study [24].

An additional exclusion criterion was applied based on our expectations for solute transport. Prior *in vivo* measurements found concentration of 3 kDa dextran to be nearly uniform within 500 µm of the cortical surface, as shown in figure 1e,f [22]. While the concentration along penetrating PVSs, measured via fluorescent intensity, was approximately constant, error bars on that measurement extending approximately ±10% of the mean indicated that there could still be some variation in solute concentration along penetrating PVSs (figure 1*f*). Accordingly, we deemed a simulation unrealistic if the average solute concentration at cortical depths of approximately 500 µm was less than 80% of the concentration in penetrating PVS prior to the first pericapillary bifurcation.

Furthermore, we simulated sleep versus wakefulness, allowing an additional criterion to be considered. The previous realism criteria were determined from experiments on anaesthetized mice, and thus are only applicable to simulations of sleep, not wakefulness. However, sleep increases glymphatic solute clearance [35] as well as flow speeds [53,54]. For solute injected directly into brain tissue, glymphatic influx rates are 1.5-fold faster [53] due to circadian rhythms alone. Similarly, solute clearance rates are up to threefold [35] faster during the early stages of sleep than during wakefulness. Thus, we propose that simulations are realistic if volume flow rates increase by at least 1.5-fold between sleep and wake.

3. Results

3.1. Simulations of solute transport by advection and diffusion

First, to characterize typical solute distributions predicted by our model, we averaged the concentrations over all segment types, producing a single-value average for each of the 1000 simulations, to estimate probability density functions (PDFs) in pial, penetrating, capillary and parenchymal segments, as shown in figure 2*a–d*. Concentrations were consistently high in the pial and penetrating segments and low in the parenchyma, with more variation in capillary PVSs. The concentration gradient $\mathcal{E}(c)$ varied similarly. As concentrations in the pial and penetrating PVSs were almost always high and concentrations in the parenchyma were low, the variation in pericapillary concentration dominated the variation in $\mathcal{E}(c)$. Since average velocities near the inlet were set to 18.7 µm s^{-1}, the volume flow rate at the inlet Q_{in} varied by only a factor of four (figure 2*f*).

While trends in average concentration were similar in realistic and excluded simulations, PDFs of realistic simulations in figure 2*a–e* had sharper peaks, implying lower variability. In particular, most simulations with small c_{pen} were unrealistic (figure 2*b*). Thus, most simulations with small $\mathcal{E}(c)$ were also unrealistic, since $\mathcal{E}(c)$ was strongly affected by the difference between c_{par}, which was always small, and c_{pen} (figure 2*b,f*). The median concentrations in each segment for realistic simulations were c_{pial} = 99.3, c_{pen} = 99.1, c_{cap}= 55.6 and c_{par}= 4.8.

Next, we considered the relative importance of advection (solute transport by bulk fluid motion) and diffusion in pial PVSs, penetrating PVSs, capillary PVSs and parenchyma. In pial and penetrating PVSs, the Péclet number (the ratio of advective to diffusive transport) typically exceeded unity, indicating that advection transported 3 kDa dextran more rapidly than diffusion, as shown in figure 2*g*. However, in capillary PVSs and the parenchyma, the Péclet number was typically less than unity, implying that diffusion transported 3 kDa dextran more rapidly than advection.

Next, we considered the fraction of solute mass, M_{frac}, found in pial PVSs, penetrating PVSs, capillary PVSs and parenchyma. Nearly all solute was found in the parenchyma, whose volume far exceeded those of PVSs, in all simulations. The median fraction of solute found in the parenchyma across all simulations was 0.9994. Pial PVSs, the vessel type which held the second greatest fraction of solute, contained at most 0.1% of the solute; penetrating and capillary PVSs contained less. The average concentration in the parenchyma is thus particularly important for characterizing solute transport.

3.2. Global sensitivity

To quantify the sensitivity of model predictions to different parameters, we computed several correlations. Figure 2*h* suggests the median parenchymal concentration c_{par} was the most important quantity for solute transport, as most solute was found in the parenchyma. Therefore, in figure 3*a*, we show the Pearson's correlation coefficient for the relationship between each input parameter and c_{par}. A coefficient magnitude close to unity indicates a strong linear correlation and whereas a coefficient near zero indicates no correlation. The pial area ratio Γ_{pial} had the greatest impact on c_{par}.

To better understand the relationship between c_{par} and Γ_{pial}, we also explored how the underlying fluid motion was influenced by the input parameters (figure 3*b,c*). Γ_{pial}, κ_{pen} and κ_{paren} had the strongest correlation with parenchymal volume flow rate Q_{par}. More significantly, the volume flow rate at the inlet Q_{in} scaled nearly linearly with Γ_{pial}. The global sensitivity of c_{par} to Γ_{pial} can be attributed to an increase in flow promoting solute transport, both by increasing flow through the parenchyma and by delivering more solute along pial and penetrating PVSs.

To further explore the relationship between input parameters and solute transport, we also calculated the correlation between $\mathcal{E}(c)$ and the input parameters. Unlike c_{par} and Q_{par}, the concentration gradient was not especially sensitive to the pial

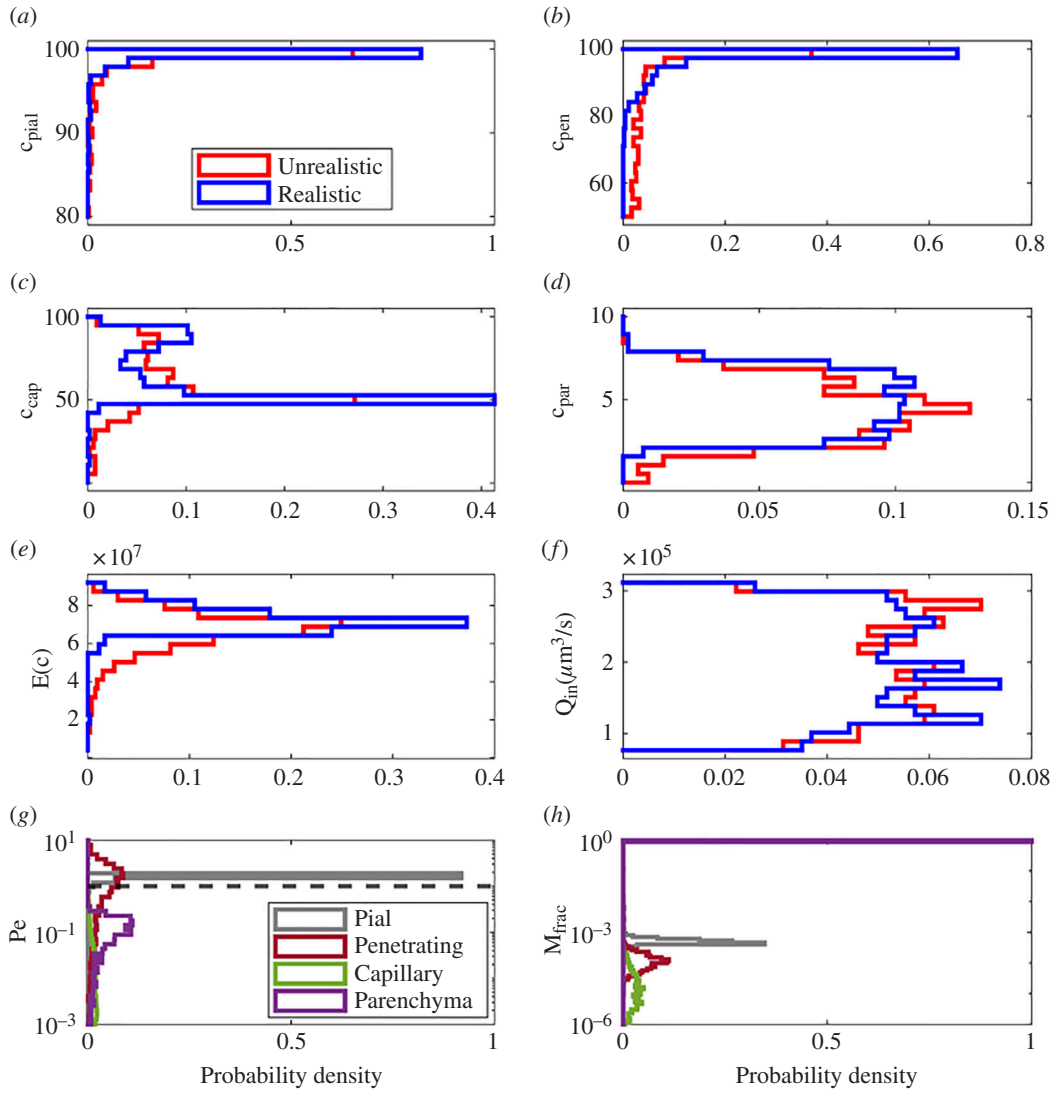

Figure 2. (*a–d*) Probability density functions (PDFs) of the average concentration in the pial perivascular spaces (c_{pial}), penetrating perivascular spaces (c_{pen}), capillary perivascular spaces (c_{cap}) and parenchyma (c_{par}). The inlet concentration of 100 provides an upper limit on concentration values in all segments of the model. (*e*) PDFs of the total concentration gradient $\mathcal{E}(c)$. (*f*) PDFs of volume flow rate through the inlet of the network (Q_{in}). In (*a–f*), simulations that satisfy all criteria for realism (blue) are compared with simulations that do not (red). (*g*) PDFs of the Péclet number Pe in the three types of perivascular spaces and the parenchyma, with $Pe = 1$ indicated with a dashed line. $Pe > 1$, implying that advection contributes significantly to solute transport, in pial perivascular spaces and in many penetrating perivascular spaces, while diffusion dominates in the parenchyma. (*h*) PDFs of the fraction of a network's total solute mass (M_{frac}) in three types of perivascular spaces and the parenchyma. In all simulations, nearly all of the solute mass in the system is found in the parenchyma.

parameters. Instead, the capillary parameters were relatively important. However, the concentration gradient of the network was not highly sensitive to any single input parameter.

3.3. Local sensitivity

To demonstrate how the sensitivity varied across the parameter space, we isolated the effect of each input parameter using a local sensitivity analysis. For each simulation shown in figures 2 and 3, we perturbed each of the 11 input parameters X_i (listed in table 1) by 5% and determined how that change affected either c_{par} or Q_{in}, both shown to be important by the global sensitivity analysis. A local sensitivity coefficient of 10 indicates that perturbing parameter X_i by 1% of its value resulted in a 10% change in c_{par} or Q_{in}.

Figure 4 shows the results. No single input parameter always induced large changes in c_{par} or Q_{in}, though each induced significant change in some simulations. This fact contrasts the prior local sensitivity analysis on hydraulic resistance [24], for which small changes in capillary parameters produced almost no change in total conductance. While we confirmed that the conductance was changing locally, per the condition on pial velocities, these alterations induced changes in the applied pressure drop. As a result, the fluid motion typically changes slightly and can change significantly in response to any change in input parameter. On average, c_{par} was much more locally sensitive to any given parameter than was Q_{in}. However, when ranking the sensitivity coefficients for each perturbation in the initial 1000 simulations, the pial efflux E_{pial} was most likely to have the

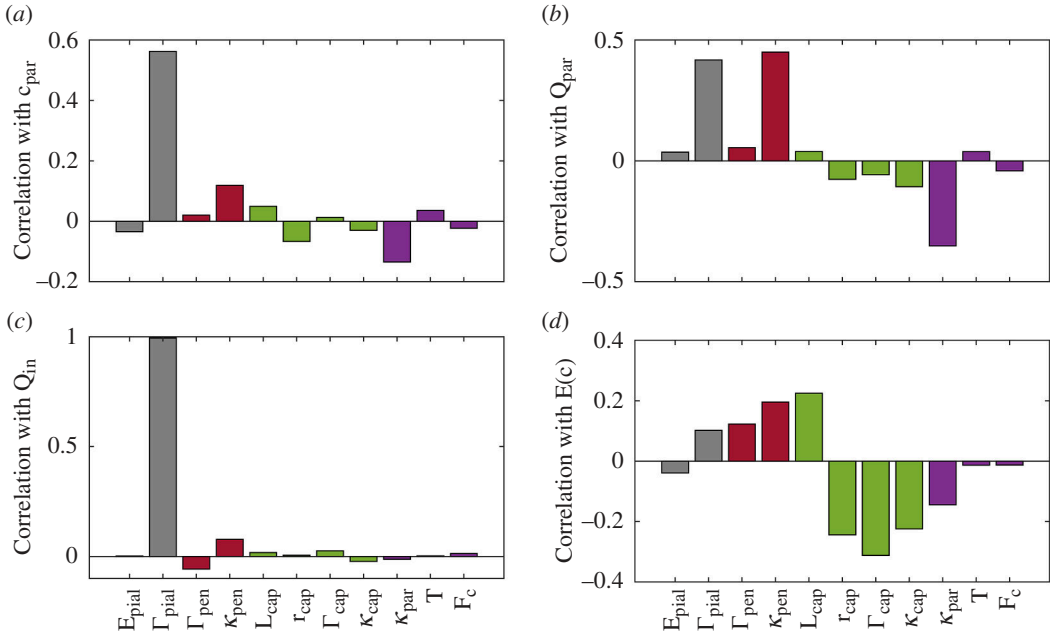

Figure 3. Pearson's correlation coefficients for (*a*) the average parenchymal concentration c_{par}, (*b*) volume flow rate through the parenchyma Q_{par}, (*c*) total volume flow rate Q_{in} and (*d*) total concentration gradient $\mathcal{E}(c)$. Parameters of pial spaces, penetrating spaces and capillary spaces are shown in grey, red and purple, respectively. Table 1 defines the symbols.

largest sensitivity coefficient for both c_{par} and Q_{in}, as shown in figure 4*b,d*. c_{par} and Q_{in} were most sensitive to changes in E_{pial} in 65.0 and 76.1% of simulations, respectively. While local changes in any of the input parameters influenced fluid and solute transport, E_{pial} had the greatest effect on Q_{in}, with implications for parenchymal solute delivery.

3.4. Parameter combinations leading to realistic predictions

Few *in vivo* measurements are available for constraining the predictions of our model, but we can use expectations about proper glymphatic function to say more about which parameter combinations lead to realistic or unrealistic predictions. Specifically, we assert that realistic predictions must have a global pressure drop less than 1 mmHg, have good CSF perfusion of brain cortex, and have near-uniform solute concentration in the outermost 500 µm of cortex (see §2). Previous research emphasized the significance of the relationship between penetrating permeability (κ_{pen}) and pial efflux (E_{pial}) for achieving realistic fluid motion [24].

Figure 5*a* shows that penetrating permeability κ_{pen} remained an important parameter in our simulations. When penetrating permeability was low, the pressure drop often exceeded 1 mmHg, an unrealistic result. While not all simulations with a low of κ_{pen} required a large pressure drop to drive realistic pial flow, nearly all simulations for which there is an unrealistically large pressure drop occurred when $\kappa_{pen} < 10^{-13}$ m^2 s^{-1}. Correspondingly, figure 5*c* shows that for $\kappa_{pen} \geq 7 \times 10^{-14}$ m^2 s^{-1}, predictions were likely to be realistic.

Similarly, we find that the parenchymal resistance R_{par} is important for realistic fluid efflux (figure 5*b*). The parenchymal resistance is the resistance through the astrocyte endfoot gaps plus the resistance in the porous tissue of the parenchyma. When the parenchymal resistance is low, fluid in the network of PVSs enters the parenchyma at the first available bifurcation, leading to poor fluid perfusion.

Figure 5*d* shows which predictions were realistic or unrealistic, depending on the permeability of penetrating PVSs, κ_{pen}, and the total parenchymal resistance, R_{par}. When both were low, no simulations made realistic predictions. This is because small κ_{pen} led to unrealistically high pressure drops, while small R_{par} led to unrealistically poor perfusion (figure 5*a,b*). The equation of the dashed line which bounds the region where all simulations are unrealistic is $\log(R_{par}) = -1.27 \times \log(\kappa_{pen}) - 24.60$, where R_{par} has units of mmHg × min ml^{-1} and κ_{pen} has units of m^2. This relationship allows us to narrow the parameter space based on the relationship between the values of R_{par} and κ_{pen}.

3.5. Simulations of sleep and wakefulness

Next, we expanded our analysis by pairing each simulation used in the global sensitivity analysis with a corresponding wakefulness simulation. To simulate wakefulness, the resistance of the parenchyma was increased to match observed sleep–wake differences in the exchange of CSF with interstitial fluid (ISF) [21]. With these paired sleep–wake simulations, we explored the network model's ability to produce the enhanced glymphatic influx that has been reported during sleep [35,53].

Figure 6*a* presents a global sensitivity analysis of the ratio of total volume flow rates during sleep and wake, Q_{sleep}/Q_{wake}. While most input parameters were not strongly correlated with Q_{sleep}/Q_{wake}, there was a negative correlation with the

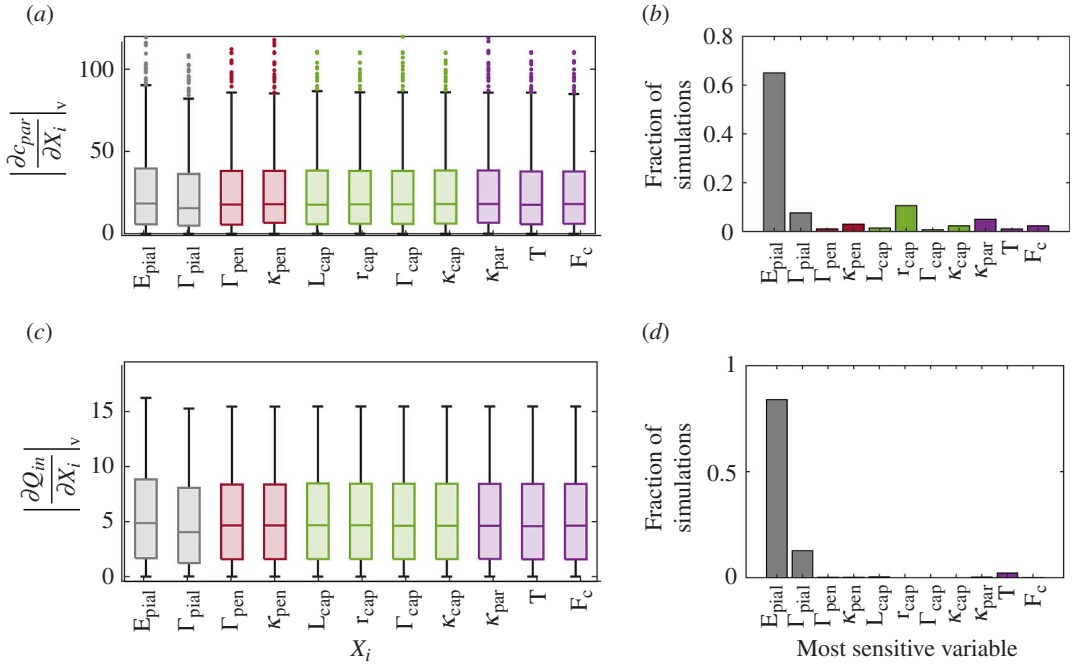

Figure 4. Local sensitivity analysis. (*a*) Local sensitivity coefficients for c_{par}. Boxes indicate the median and interquartile range, while whiskers indicate the 5th and 95th percentiles and dots show outliers. (*b*) Fraction of simulations in which each parameter, of the 11, has the greatest sensitivity coefficient for c_{par}. (*c*) Local sensitivity coefficients for Q_{in}. (*d*) Fraction of simulations in which each parameter has the greatest sensitivity coefficient for Q_{in}. Table 1 defines the symbols.

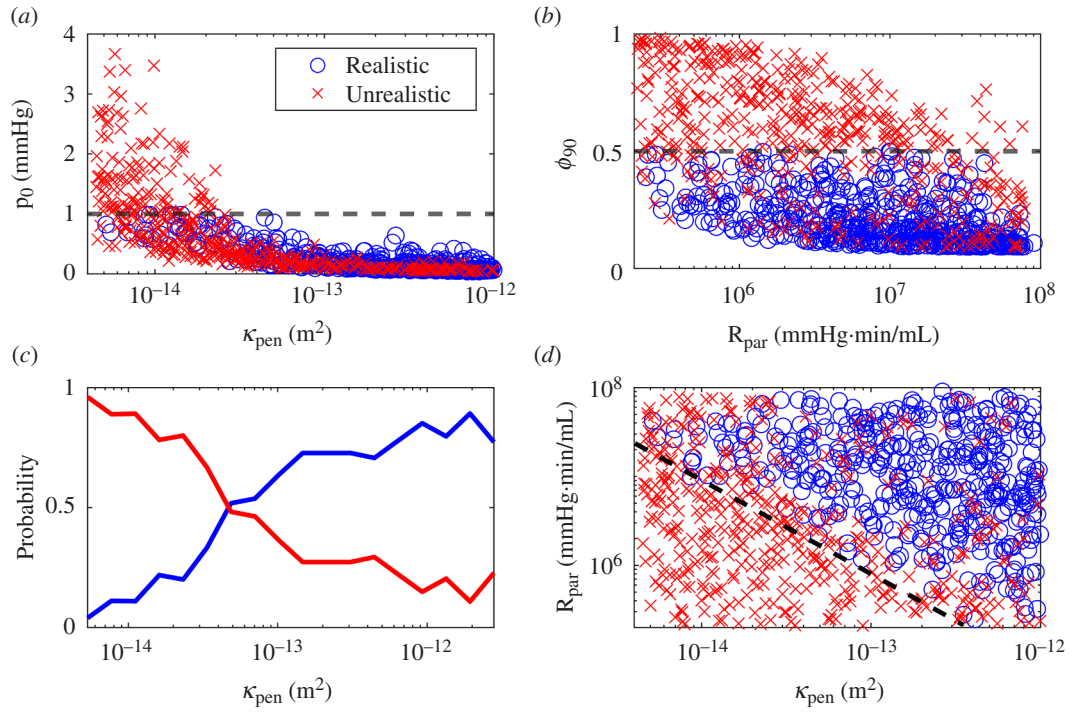

Figure 5. Realism of predictions depends heavily on penetrating permeability. (*a*) Total pressure drop p_0 varying with penetrating permeability κ_{pen}, over all simulations. As in figure 2, realistic and unrealistic simulations are plotted in blue and red, respectively. Simulations with $p_0 > 1$ mmHg are always deemed unrealistic. (*b*) Fraction of fluid which exits the perivascular spaces at the first bifurcation along penetrating PVSs, ϕ_{90}, varying with R_{par}. Realistic and unrealistic simulation results are plotted blue and red, respectively. Simulations with $\phi_{90} > 0.5$ are always deemed unrealistic. (*c*) The probability of a simulation being realistic increases rapidly with κ_{pen}. (*d*) Total parenchymal resistance R_{par} varying with κ_{pen}. The model is much more likely to produce realistic results when the penetrating perivascular spaces are highly permeable and the parenchyma is highly resistive. The dashed line denotes the region for which no simulations are realistic.

parenchymal permeability κ_{par}. Figure 6*b* shows Q_{sleep}/Q_{wake} and κ_{par} for each simulation. Large parenchymal permeability apparently prohibited substantial sleep–wake flow variation. Figure 6*c* demonstrates that the ratio of concentration in the parenchyma during sleep and wake, $c_{par,\,sleep}/c_{par,\,wake}$, and Q_{sleep}/Q_{wake} tended to scale with each other. There are some simulations for which the flow rate ratio exceeded the parenchymal concentration ratio. This effect was previously found to be caused by a significant portion of the fluid being directed into capillary pathways [21].

To further explore the effect of parenchymal resistance on solute transport, figure 6*d,e* depicts how $c_{par,sleep}/c_{par,wake}$ varied with the total parenchymal resistance and the ratio of parenchymal resistances during sleep and wake. $c_{par,sleep}/c_{par,wake}$ tended to increase with $R_{par,sleep}$ and was never large when $R_{par,sleep}$ was small. Since brain tissue resistance varies inversely with κ_{par}, this trend is related to the weakly linear relationship shown in figure 6*a,b*. Figure 6*e* demonstrates that relative sleep-to-wake parenchymal solute concentration tended to increase only if the relative sleep-to-wake parenchymal resistance significantly increased. The total parenchymal resistance $R_{par,sleep}$ was the sum of the resistance to flow through endfoot gaps and the resistance to flow through brain tissue, as these resistances are in series in this model (figure 1*c*). Since only the resistance of the tissue was increased for wakefulness simulations, if $R_{par,wake}/R_{par,sleep} \sim 1$, the resistance of the endfoot gaps was much greater than the resistance of the brain tissue. In this scenario, the sleep–wake variations in tissue permeability had less impact on solute transport.

3.6. Sleep, wakefulness and realism of predictions

Next, we considered $Q_{sleep}/Q_{wake} > 1.5$ as its own exclusion criterion, based on the expectation of increased volume flow rates in pial spaces according to circadian rhythms [53]. First, we examined the values of Q_{sleep}/Q_{wake} in simulations deemed realistic or unrealistic based on the original three criteria (pressure drop less than 1 mmHg, good fluid perfusion, and near-constant solute concentration along the penetrating PVSs). As shown in figure 7*a,b*, Q_{sleep}/Q_{wake} depends on the penetrating permeability κ_{pen} and the parenchymal resistance R_{par}. Q_{sleep}/Q_{wake} was small when the penetrating PVSs were less permeable (corresponding to high resistance), and when the parenchymal resistance was less than 10^6. It is worth noting that R_{par} depends on both the resistance to flow through the endfoot gaps as well as resistance to Darcy flow through the porous brain tissue. Interestingly, simulations with $Q_{sleep}/Q_{wake} > 1.5$ were also more likely to be deemed realistic based on the original three criteria, which pertain to the fluid and solute behaviour (figure 7*c*).

When using $Q_{sleep}/Q_{wake} > 1.5$ as the sole criterion for realism, we found that simulations were much more likely to be realistic when κ_{pen} was high and R_{par} was high (figure 7*d*). The dashed line is specified by $\log(R_{par}) = -1.07 \times \log(\kappa_{pen}) - 15.15$, a relationship intriguingly similar to the one in figure 5*d*, although fewer simulations had an appropriate Q_{sleep}/Q_{wake} compared with those that simply met the realistic solute and fluid transport criteria. As the pressure drop was the same for the paired sleep–wake simulations, changes in volume flow rate were caused by changes in resistance. When the parenchyma had a higher resistance, changing its permeability by a factor of 5.5 could induce a greater change in the model's resistance, since the parenchymal resistance was larger than the astrocyte endfoot resistance, thus increasing Q_{sleep}/Q_{wake}. That said, those sleep–wake changes in parenchymal resistance could strongly affect the global volume flow rate only if resistances elsewhere were relatively low. Low-resistance penetrating PVSs are possible only with large κ_{pen}, which affects resistance more than any other parameter [24]. Thus, realistic sleep–wake variation of volume flow rate requires that both R_{par} and κ_{pen} be large.

3.7. Model sensitivity as a function of outlet concentration

Until this point, we have modelled the injection of a dye that is rapidly removed from the parenchyma along efflux routes where the solute concentration is assumed to be zero. This assumption is common in glymphatic modelling [25,36]. However, efflux is difficult to measure *in vivo* and the exact concentration along efflux routes remains unknown. To explore the implications of this uncertainty, we performed additional simulations, setting the concentration at the outlet c_{out} to 10, 25 or 50, leaving other parameters unchanged.

Figure 8*a* shows PDFs of the average parenchymal concentration as the outlet concentration was increased. For the $c_{out} = 0$ simulations, the average parenchymal concentration was always low, with a median value of 4.3. However, when $c_{out} > 0$, the median parenchymal concentration dramatically increased, climbing to 46.8, 56.6 and 70.7 when c_{out} was 10, 25, and 50, respectively. The sensitivity of solute transport to input parameters also depended on c_{out}. Figure 8*b* repeats figure 3*a*, and figure 8*c–e* shows the same correlation coefficients when c_{out} was 10, 25 and 50, respectively. As c_{out} increased, Γ_{pial} became less important. Figure 8*c,d* shows that when $0 < c_{out} < 50$, Γ_{pial}, κ_{pen} and κ_{par} were relatively important, though their correlation coefficients never exceeded 0.4 in magnitude. Figure 8*e* shows that as the outlet concentration continued to increase, approaching the inlet concentration, the model became less sensitive to input parameters, as expected. These findings suggest that without a low-concentration efflux path, parenchymal solute concentration remains high and good clearance is not possible, regardless of parameter values.

4. Discussion

In this sensitivity analysis, we found that pial area ratio Γ_{pial} and pial efflux E_{pial} are important parameters for fluid and solute behaviour throughout the network. Additionally, the permeability in parenchymal κ_{par} and penetrating spaces κ_{pen} are important in determining whether a model will have realistic fluid and solute transport properties. In fact, we can narrow our parameter space to exclude simulations for which the ratio of penetrating permeability to parenchymal resistance is small. Even with the variations in solute transport behaviour induced by these four parameters, over the time required to reach steady state, the solute tends to saturate the pial and penetrating PVSs, with concentrations in the pericapillary and parenchymal spaces

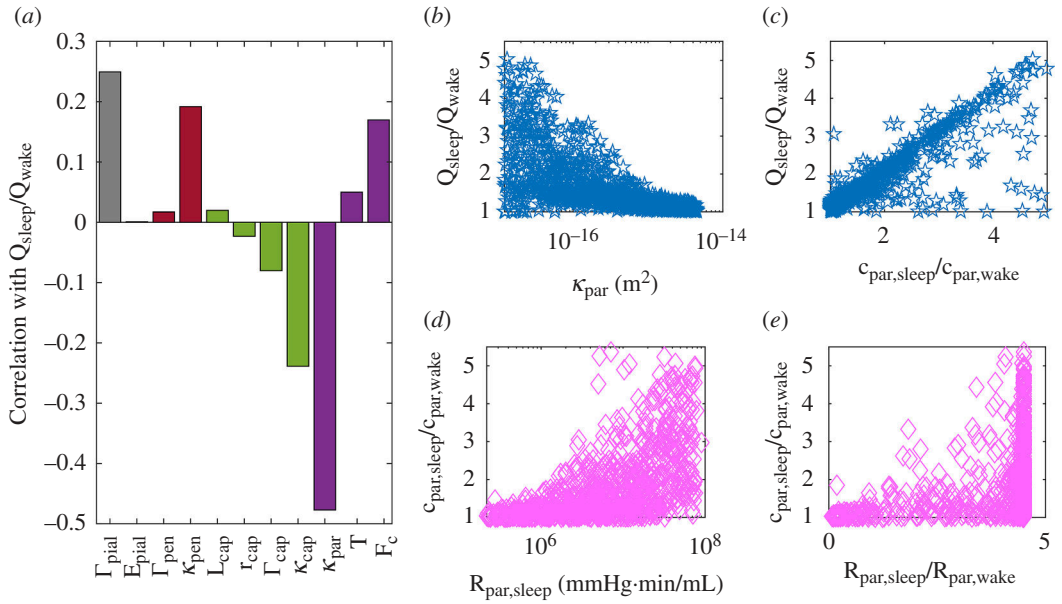

Figure 6. Simulations of sleep and wakefulness for realistic fluid and solute conditions. (*a*) Pearson's correlation coefficients of the ratio of total volume flow rates during sleep and wake, Q_{sleep}/Q_{wake}. Table 1 defines the symbols. (*b*) Variation of Q_{sleep}/Q_{wake} with parenchymal permeability κ_{par}. When the parenchymal permeability is lower, sleep-associated changes in the parenchymal resistance can induce a larger difference in volume flow rate. (*c*) Q_{sleep}/Q_{wake} is often nearly identical to the ratio of mean parenchymal concentrations during sleep and wake, $c_{par,\,sleep}/c_{par,\,wake}$. (*d*) $c_{par,\,sleep}/c_{par,\,wake}$ varying with parenchymal resistance of simulations of sleep, $R_{par,\,sleep}$. Large $R_{par,\,sleep}$ allows greater variability in $c_{par,\,wake}$. (*e*) Variation of $c_{par,\,sleep}/c_{par,\,wake}$ with the ratio of parenchymal resistances in wake and sleep, $R_{par,\,wake}/R_{par,\,sleep}$.

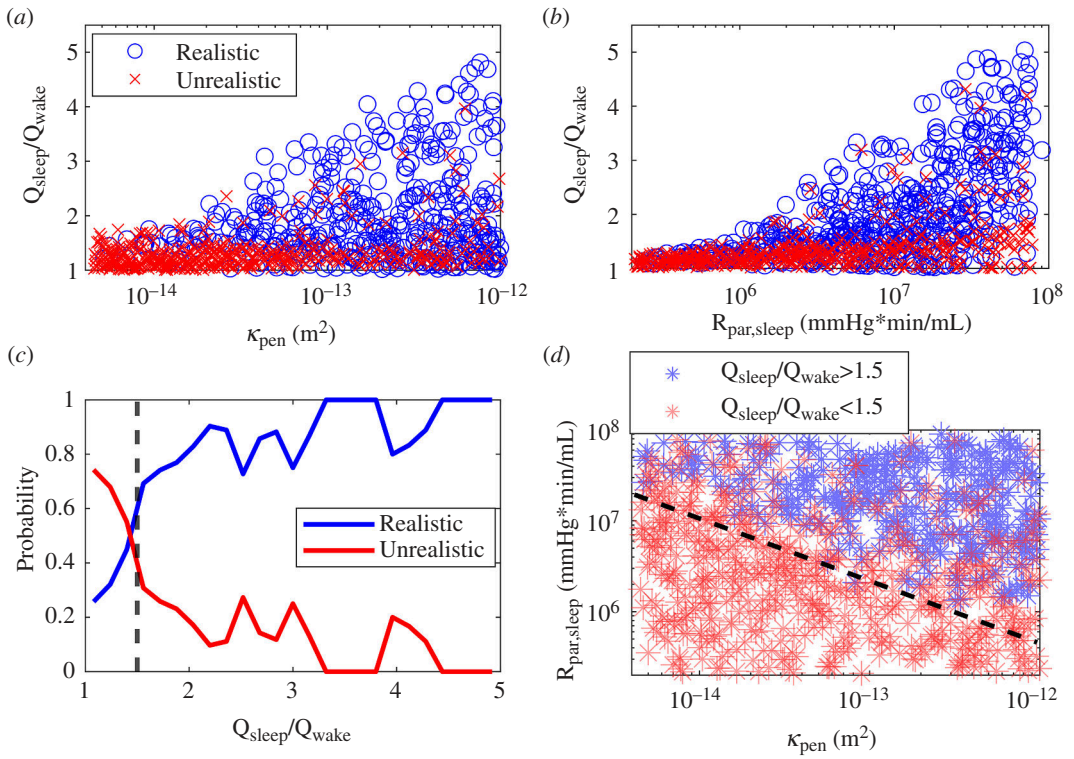

Figure 7. Variation of volume flow rates between simulations of sleep and wakefulness. (*a*) Q_{sleep}/Q_{wake} varies with penetrating PVS permeability, κ_{pen}. When κ_{pen} is high, simulations are usually realistic and Q_{sleep}/Q_{wake} is often large. (*b*) Q_{sleep}/Q_{wake} varies with the resistance of the parenchyma during sleep, $R_{par,\,sleep}$. Large Q_{sleep}/Q_{wake} occurs only if $R_{par,\,sleep}$ is high. (*c*) The probability of a simulation exhibiting realistic sleep behaviour, as a function of Q_{sleep}/Q_{wake}. A dashed line indicates $Q_{sleep}/Q_{wake} = 1.5$. Simulations for which Q_{sleep}/Q_{wake} is large are more likely to be realistic. (*d*) R_{par} varying with κ_{pen}, over all simulationscoloured based on whether Q_{sleep}/Q_{wake} is realistic. A dashed line bounds the region for which no simulations are realistic.

decreasing due to the 0 concentration boundary condition at the outlets. When the concentration at the outlets is allowed to increase, parenchymal concentration becomes less strongly dependent on individual model parameters.

In most realistic simulations, the average concentration in the pial and penetrating spaces is close to 100, the inlet concentration. The high average concentration in these spaces is, in part, the result of high average Péclet numbers. In figure 2*e–h*, the

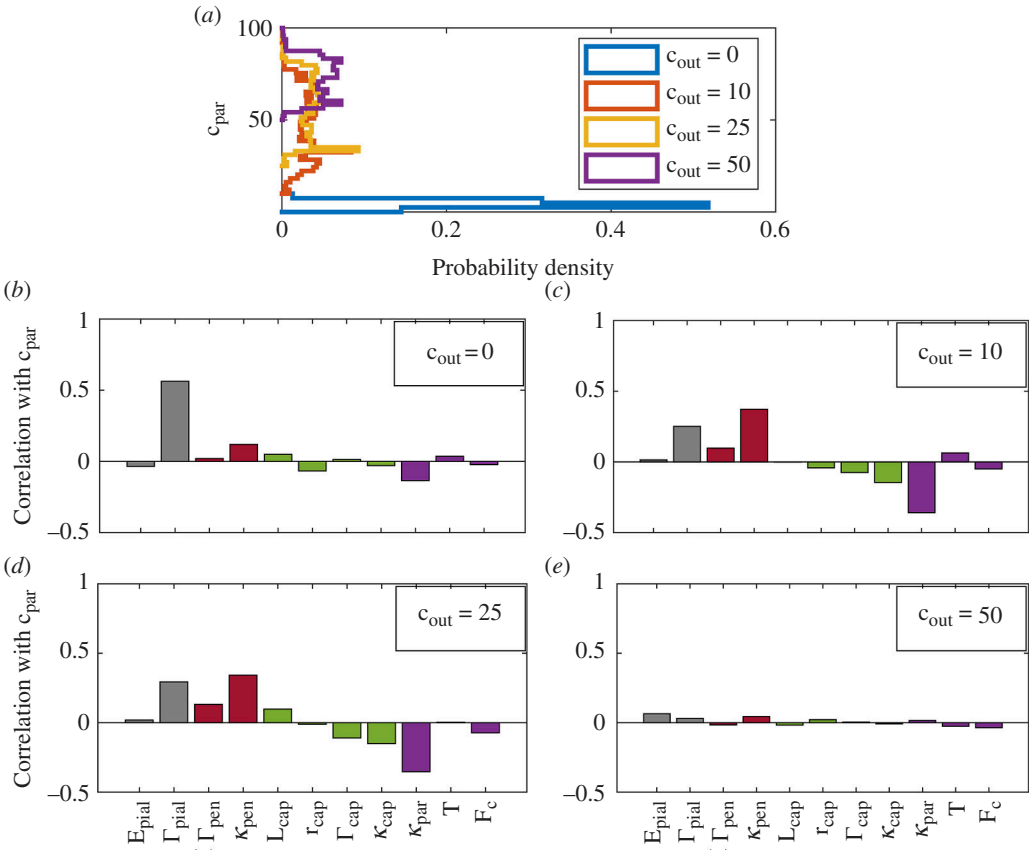

Figure 8. Parenchymal concentration and parameter sensitivity depend on specified outlet concentration. (*a*) Probability densities of parenchymal concentration c_{par} for varying outlet concentration boundary conditions, c_{out}. Typically, c_{par} increases with c_{out}. (*b–e*) Pearson's correlation coefficients for c_{par}, with varying c_{out}. As c_{out} increases, sensitivity decreases, especially for Γ_{pial}. Table 1 defines the variable symbols.

Péclet numbers indicate that solute transport in penetrating PVSs is usually dominated by advection, while solute transport in the parenchyma is always dominated by diffusion. This is consistent with previous estimates of solute transport [38,55]. Necessarily, there is little variation in the Péclet number along pial PVSs, as the mean velocity in the first third of the model is set. In a PVS segment where transport is purely due to advection ($Pe = \infty$), equation (2.1) simplifies to

$$u\frac{\partial c}{\partial z} = 0. \tag{4.1}$$

Thus, we expect segments with a high Péclet number to have a near-constant concentration. In the case where several advection-dominated segments are connected to the inlet, all such segments should have an average concentration nearly equal to the inlet concentration, according to equation (4.1). While the Péclet numbers are not generally high enough that diffusion is completely negligible, the reasonably large Péclet numbers combined with a large concentration gradient between the inlet and outlets help transport solute along PVSs and into the parenchyma and capillary PVSs. Additionally, the solute modelled is a dextran with a low molecular weight, which is highly diffusive. Many solutes naturally produced in the brain have lower diffusion coefficients. For such solutes, the Péclet number will be greater than what we report for this study. Lastly, despite the uncertainty in input parameters, in figure 2, the PDF peaks sharpen when realistic solute transport criteria are considered. Thus, our model predicts similar transport of injected solutes without strong dependence on parameters.

One important consideration in this model is the role of the diffusion coefficient in simulations. The diffusion coefficients used in this sensitivity analysis were determined experimentally [37,56]. Quantifying diffusion coefficients within brain tissue presents challenges, with observed variability suggesting that the actual diffusion coefficient of 3 kDa dextran may deviate by approximately ±10% from the mean value used in these simulations [37]. However, across the range of parameters used in the sensitivity analysis, solute transport was nearly always dominated by advection in the PVSs and diffusion in the parenchyma (figure 2*g*). Thus, varying the diffusion coefficient by 10% will have negligible impact on transport within the PVSs. Varying the diffusion coefficient in the parenchyma within that small range will increase or decrease the parenchymal concentration according to equation (2.4). This predictable change to parenchymal concentration would not substantially change network-wide solute transport or the correlations between model parameters. Thus, in this sensitivity analysis, we varied only parameters of physical brain geometry, not diffusion coefficients.

Similarly, for solutes much larger than 3 kDa dextran, we expect advection to play a larger role. Some proteins found in brain tissue, such as Ovalbumin, have an effective diffusion coefficient an order of magnitude smaller than that of 3 kDa dextran [56], causing diffusion to play a relatively smaller role in transport. Since advection dominates in most PVSs even for 3 kDa dextran, we predict the same solute transport in PVSs for any solutes with a smaller diffusion coefficient. Only the relative importance of diffusion in the parenchyma will change. However, for molecules more diffusive than 3 kDa dextran, such as sucrose or various

ions in the brain [56], diffusion will hold greater relative importance across the network. For sufficiently small solutes, advection will no longer dominate in most PVSs. This may lead to simulations in which the PVSs do not saturate with solute, and instead, the concentration in PVSs decreases significantly further away from the inlet. Solute transport into the parenchyma depends both on advection in the parenchyma and on the inlet PVS concentration (equation (2.4)). Thus, for small, highly diffusive molecules, solute transport from the inlet to brain tissue would be reduced.

The total mass in the network, dominated by parenchymal concentrations, is linearly sensitive to Γ_{pial} (figure 3). This sensitivity is caused by the linear relationship between total volume flow rate through the model and the area of the PVS at the inlet. Since the resistance of pericapillary spaces is high relative to the resistance of the parenchyma, increasing the volume flow rate at the inlet typically increases the volume flow rate in the parenchyma as well. Moreover, increasing the volume flow rate causes advection to play a greater role in the pial and penetrating spaces, assisting in the delivery of solute to the parenchyma. Interestingly, pial PVS area is known to increase with age and in humans, possibly due to inflammation [57], making this parameter particularly important for simulations of healthy and diseased brain states. However, Γ_{pial} is less important if the boundary condition at the outlet of the parenchyma is greater than zero, as is shown in figure 8. When the inlet and outlet concentrations differ less, parameters affect the parenchymal concentration less. We also see in the local sensitivity analysis (figure 4) that small changes in E_{pial} are more likely to significantly affect c_{par}. The local sensitivity coefficient is independent of the uncertainties in the parameter range. Of all input parameters, increases in E_{pial} result in the greatest increase in volume flow rate through the network. Thus, Γ_{pial} and E_{pial} are the uncertain parameters that are most likely to influence solute transport.

We find that there are nonlinear correlations between the two criteria for realistic fluid motion and the parameters κ_{pen} and R_{par} (figure 5). The pressure drop depends strongly on κ_{pen}, which is consistent with results reported in Boster *et al*. [24]. R_{par} depends on a combination of parenchymal permeability, endfoot cavity fraction and endfoot wall thickness. When the resistance to flow into the parenchyma from penetrating PVSs is lower, fluid is more likely to exit penetrating PVSs near the surface of the brain, leading to poor fluid perfusion. From this, we identified a region of parameter space for which no realistic simulations could occur.

We find that realistic sleep–wake behaviour depends on appropriate values of both parenchymal resistance to penetrating permeability. Figure 6 shows that in simulations of glymphatic transport in sleeping mice, the sleep-associated increase in volume flow rate and corresponding increase in parenchymal solute concentration depend on the permeability of the parenchyma. While the relationships are not linear, figure 6 shows that for low parenchymal resistance, the concentration in the parenchyma does not increase much during sleep. However, if parenchymal resistance is larger, the increase in resistance during wakefulness significantly affects the volume flow rate (figure 6*b*,*e*). This parameter is inversely related to κ_{par}. While the solute transport quantities were not shown to be highly linearly sensitive to κ_{par} during the initial sensitivity analysis (figure 3), for accurate sleep–wake simulations improved measurements of κ_{par} are necessary.

The parenchymal resistance depends on the resistance to flow through brain tissue and through the endfoot sheath. Previously, the resistance to flow through gaps in astrocyte endfeet was estimated to significantly hinder fluid and solute transport out of the vessel. Specifically, the effective diffusion coefficient was approximately an order of magnitude greater in astrocyte endfoot sheaths compared with brain tissue [58]. Similarly, we found that the resistance per length of astrocyte endfoot gaps is large relative to the resistance per unit length in brain tissue. In our simulations, the astrocyte endfoot sheath is two or three orders of magnitude thinner than the simulated brain tissue region, having a thickness of only 0.2–1 µm. Nevertheless, a mean of 8.9% of the total parenchymal resistance R_{par} is attributed to R_{AE} in sleep simulations. Figure 6*e* shows that solute concentrations in the parenchyma rarely increase significantly unless $R_{par,\,sleep}/R_{par,\,wake} > 4.5$. This corresponds to a sleep simulation where R_{AE} contributes at most 28.6% of the total R_{par}. While the endfoot gap resistance per length is large compared with the resistance of brain tissue or of PVSs, the thickness of the brain tissue ultimately allows tissue resistance to dominate R_{par}, producing realistic sleep–wake variations in CSF–ISF exchange when the tissue permeability is changed.

Additionally, the sleep–wake behaviour shown in figure 7 reveals a similarity between simulations that accurately reproduce fluid and solute transport in a sleeping mouse model (labelled 'realistic') and simulations that accurately reproduce variation of volume flow rate from sleep to wake (i.e. large Q_{sleep}/Q_{wake}). The most striking similarity is between figure 7*d* and figure 5*d*. The simulations that exhibit realistic fluid and solute motion in a simulation of sleep also predict a large increase in volume flow rate for sleep conditions compared to awake conditions. Parameter combinations with a high ratio of parenchymal and penetrating PVS resistances result in realistic fluid behaviour (pressure drops and fluid perfusion) and realistic solute behaviour (sleep–wake flow ratios). Specifically, simulations with appropriate fluid and solute transport can only occur if $\log(R_{par}) \geq -1.27 \times \log(\kappa_{pen}) - 24.60$ (figure 5*d*), and simulations with appropriate sleep–wake flow increases occur only for $\log(R_{par}) \geq -0.42 \times \log(\kappa_{pen}) - 26.15$ (figure 7*d*). Within the range of parenchymal permeabilities estimated for the murine brain, the condition on sleep–wake volume flow rates is more restrictive, leading to fewer realistic simulations (figures 5*d* and 7*d*). The fact that the sleep–wake criteria result in both realistic fluid and solute transport increases confidence that our model captures the real murine brain.

Finally, as the concentration boundary conditions at the outlets increase, the concentration in the parenchyma increases and the distribution widens with no strong correlations to any input parameter (figure 8). This scenario simulates slower waste clearance through perivenous efflux routes, for which the steady-state concentration within perivenous spaces would be greater than zero. Currently, velocities in perivenous spaces have not been measured, making estimations about clearance rates challenging. Additionally, in many imaging modalities the concentration of solute in the parenchyma following a dye injection into the cisterna magna is too low to differentiate from background noise [38,59]. This suggests that the outlet concentration and the average concentration in the parenchyma should remain low, but makes quantitative assessments of modelled parenchymal

concentrations challenging. Further investigation of perivenous clearance would help elucidate the appropriate boundary condition for representations of dye injections.

Since this model explores solute transport though fluid pathways that have not been well characterized *in vivo*, there are several important limitations to the study. First, little is known about capillary PVSs; even their existence is debated. Fortunately, the parenchymal and penetrating concentrations (figure 3) are not highly dependent on any of the capillary parameters, and include a wide range of capillary resistances. Second, the capillary effective length L_{cap} used in the model (table 1) is the length necessary to produce the appropriate hydraulic resistance, not necessarily the length over which advection and diffusion occur. While the calculated concentrations in the capillary segments (figure 2) may not be representative of real capillary PVSs, the response of the parenchymal and penetrating segments to changes in capillary parameters (figure 3) is appropriate.

Furthermore, this is a steady-state, 1D model, and many potential drivers of flow depend on time and higher-dimensional geometry. As a 1D model, it cannot include Taylor dispersion, which drives solute transport when both advection and diffusion are present [60], except by using an inflated diffusivity. Oscillatory pressure gradients caused by arterial motion are capable of driving some amount of the net flow in PVSs [61,62]. Additionally, arterial pulsations may be important in pushing fluid and solutes into the parenchyma from PVSs [18]. Fluid motion caused by arterial pulsations, whether associated with the cardiac cycle [7,8] or with functional hyperemia [10,63], cannot be accounted for in a time-independent model. Nor can transitions between brain states, such as sleep and wake, or transient responses, such as those that follow stroke [64] or cardiac arrest [65]. Upgrading the model to allow time-dependent simulations would broaden its applicability.

5. Conclusions

Models can provide insights into fluid and solute transport in regions of the brain that are hard to explore experimentally. Low-fidelity models such as the hydraulic resistance model used here do not closely resemble an actual biological system, but are highly computationally efficient allowing for thousands of repeated simulations. Low-fidelity models are particularly useful for systems where the geometry of fluid pathways is not sufficiently characterized to develop accurate high-dimensional models. These results can then guide researchers performing *in vivo* experiments to identify which of the many difficult measurements are necessary for creating accurate simulations, and to prioritize those measurements accordingly.

In this analysis, we identify four parameters that significantly affect solute transport through PVSs and brain tissue: Γ_{pial}, E_{pial}, κ_{pen} and κ_{par}. Of these, Γ_{pial} is the easiest to measure *in vivo*. Recently, Γ_{pial} was quantified more accurately in mice [40] and in humans [14]. However, E_{pial}, κ_{pen} and κ_{par} are equally important parameters for model behaviour which will be more challenging to measure. While solute transport is not linearly sensitive to κ_{pen} in our model, pressure drop and sleep–wake variation are sensitive. In simulations where the permeability of the penetrating PVSs is low, Q_{sleep}/Q_{wake} is often low as well, indicating that the model is unrealistic. The investigation into the relationship between κ_{pen} and realistic fluid and solute motion in figure 5 emphasizes the significance of this parameter in the network model. Simulating repeatedly, we found almost no realistic predictions when $\kappa_{pen} < 10^{-14}$ m^2, so we conjecture that future measurements will indeed find the permeability of penetrating PVSs to exceed this value. We conclude that measurements of E_{pial}, κ_{pen} and κ_{par} must be performed *in vivo* so that more accurate, higher dimensional solute transport models can be created.

Ethics. This work did not require ethical approval from a human subject or animal welfare committee.

Data accessibility. Simulation code with sample parameter sets and visualization code is available at Zenodo [66].

Declaration of AI use. We have not used AI-assisted technologies in creating this article.

Authors' contributions. K.Q.: conceptualization, methodology, software, visualization, writing—original draft, writing—review and editing; K.A.S.B.: methodology, software, writing—review and editing; J.T.: software, writing—review and editing; D.H.K.: conceptualization, supervision, writing—original draft, writing—review and editing.

All authors gave final approval for publication and agreed to be held accountable for the work performed therein.

Conflict of interest declaration. We declare we have no competing interests.

Funding. This work was supported by the US Army (grant no. MURI W911NF1910280), by the US National Center for Complementary and Integrative Health (grant no. R01AT012312) and by the BRAIN Initiative of the US National Institutes of Health (under grant no. U19NS128613). J.T. holds a Career Award at the Scientific Interface from Burroughs Wellcome Fund.

Acknowledgements. We thank Yiming Gan for advice about numerical methods.

References

1. Camandola S, Mattson MP. 2017 Brain metabolism in health, aging, and neurodegeneration. *EMBO J*. **36**, 1474–1492. (doi:10.15252/embj.201695810)
2. Wagshul ME, Johnston M. 2013 The brain and the lymphatic system. In *Immunology of the lymphatic system*, pp. 143–164. New York, NY: Springer. (doi:10.1007/978-1-4614-3235-7_8)
3. Milhorat TH. 1975 The third circulation revisited. *J. Neurosurg*. **42**, 628–645. (doi:10.3171/jns.1975.42.6.0628)
4. Rennels ML, Gregory TF, Blaumanis OR, Fujimoto K, Grady PA. 1985 Evidence for a 'paravascular' fluid circulation in the mammalian central nervous system, provided by the rapid distribution of tracer protein throughout the brain from the subarachnoid space. *Brain Res.* **326**, 47–63. (doi:10.1016/0006-8993(85)91383-6)
5. Iliff JJ, Wang M, Zeppenfeld DM, Venkataraman A, Plog BA, Liao Y, Deane R, Nedergaard M. 2013 Cerebral arterial pulsation drives paravascular CSF-interstitial fluid exchange in the murine brain. *J. Neurosci*. **33**, 18190–18199. (doi:10.1523/JNEUROSCI.1592-13.2013)

6. Iliff JJ, Lee H, Yu M, Feng T, Logan J, Nedergaard M, Benveniste H. 2013 Brain-wide pathway for waste clearance captured by contrast-enhanced MRI. *J. Clin. Invest*. **123**, 1299–1309. (doi:10.1172/JCI67677)
7. Mestre H *et al*. 2018 Flow of cerebrospinal fluid is driven by arterial pulsations and is reduced in hypertension. *Nat. Commun*. **9**, 4878. (doi:10.1038/s41467-018-07318-3)
8. Raghunandan A, Ladron-de-Guevara A, Tithof J, Mestre H, Du T, Nedergaard M, Thomas JH, Kelley DH. 2021 Bulk flow of cerebrospinal fluid observed in periarterial spaces is not an artifact of injection. *eLife* **10**, e65958. (doi:10.7554/eLife.65958)
9. Cai X, Qiao J, Kulkarni P, Harding IC, Ebong E, Ferris CF. 2020 Imaging the effect of the circadian light-dark cycle on the glymphatic system in awake rats. *Proc. Natl Acad. Sci. USA* **117**, 668–676. (doi:10.1073/pnas.1914017117)
10. Holstein-Rønsbo S *et al*. 2023 Glymphatic influx and clearance are accelerated by neurovascular coupling. *Nat. Neurosci*. **26**, 1042–1053. (doi:10.1038/s41593-023-01327-2)
11. Benveniste H, Elkin R, Heerdt PM, Koundal S, Xue Y, Lee H, Wardlaw J, Tannenbaum A. 2020 The glymphatic system and its role in cerebral homeostasis. *J. Appl. Physiol.***129**, 1330–1340. (doi:10.1152/japplphysiol.00852.2019)
12. Bèchet NB, Shanbhag NC, Lundgaard I. 2021 Glymphatic pathways in the gyrencephalic brain. *J. Cereb. Blood Flow Metab*. **41**, 2264–2279. (doi:10.1177/0271678X21996175)
13. Young BA, Adams J, Beary JM, Mardal KA, Schneider R, Kondrashova T. 2021 Variations in the cerebrospinal fluid dynamics of the American alligator (*Alligator mississippiensis*). *Fluids Barriers CNS* **18**, 11. (doi:10.1186/s12987-021-00248-1)
14. Eide PK, Vinje V, Pripp AH, Mardal KA, Ringstad G. 2021 Sleep deprivation impairs molecular clearance from the human brain. *Brain* **144**, 863–874. (doi:10.1093/brain/awaa443)
15. Fultz NE, Bonmassar G, Setsompop K, Stickgold RA, Rosen BR, Polimeni JR, Lewis LD. 2019 Coupled electrophysiological, hemodynamic, and cerebrospinal fluid oscillations in human sleep. *Science* **366**, 628–631. (doi:10.1126/science.aax5440)
16. Myllylä T, Harju M, Korhonen V, Bykov A, Kiviniemi V, Meglinski I. 2018 Assessment of the dynamics of human glymphatic system by near-infrared spectroscopy. *J. Biophotonics* **11**, e201700123. (doi:10.1002/jbio.201700123)
17. Mehta NH *et al*. 2022 Quantifying cerebrospinal fluid dynamics: a review of human neuroimaging contributions to CSF physiology and neurodegenerative disease. *Neurobiol. Dis*. **170**, 105776. (doi:10.1016/j.nbd.2022.105776)
18. Daversin-Catty C, Vinje V, Mardal KA, Rognes ME. 2020 The mechanisms behind perivascular fluid flow. *PLoS One* **15**, e0244442. (doi:10.1371/journal.pone.0244442)
19. Bork PA, Ladrón-de-Guevara A, Christensen AH, Jensen KH, Nedergaard M, Bohr T. 2023 Astrocyte endfeet may theoretically act as valves to convert pressure oscillations to glymphatic flow. *J. R. Soc. Interface* **20**, 20230050. (doi:10.1098/rsif.2023.0050)
20. Faghih MM, Sharp MK. 2018 Is bulk flow plausible in perivascular, paravascular and paravenous channels? *Fluids Barriers CNS* **15**, 17. (doi:10.1186/s12987-018-0103-8)
21. Tithof J, Boster KAS, Bork PAR, Nedergaard M, Thomas JH, Kelley DH. 2022 A network model of glymphatic flow under different experimentally-motivated parametric scenarios. *iScience* **25**, 104258. (doi:10.1016/j.isci.2022.104258)
22. Mestre H *et al*. 2018 Aquaporin-4-dependent glymphatic solute transport in the rodent brain. *eLife* **7**, e40070. (doi:10.7554/eLife.40070)
23. Blinder P, Tsai PS, Kaufhold JP, Knutsen PM, Suhl H, Kleinfeld D. 2013 The cortical angiome: an interconnected vascular network with noncolumnar patterns of blood flow. *Nat. Neurosci*. **16**, 889–897. (doi:10.1038/nn.3426)
24. Boster KA, Tithof J, Cook DD, Thomas JH, Kelley DH. 2022 Sensitivity analysis on a network model of glymphatic flow. *J. R. Soc. Interface* **19**, 20220257. (doi:10.1098/rsif.2022.0257)
25. Mukherjee S, Tithof J. 2022 Model of glymphatic clearance of aggregating proteins from the brain interstitium. *Phys. Rev. E* **105**, 024405. (doi:10.1103/PhysRevE.105.024405)
26. Martinac AD, Bilston LE. 2020 Computational modelling of fluid and solute transport in the brain. *Biomech. Model. Mechanobiol*. **19**, 781–800. (doi:10.1007/s10237-019-01253-y)
27. Thomas JH. 2022 Theoretical analysis of wake/sleep changes in brain solute transport suggests a flow of interstitial fluid. *Fluids Barriers CNS* **19**, 30. (doi:10.1186/s12987-022-00325-z)
28. Troyetsky DE, Tithof J, Thomas JH, Kelley DH. 2021 Dispersion as a waste-clearance mechanism in flow through penetrating perivascular spaces in the brain. *Sci. Rep*. **11**, 4595. (doi:10.1038/s41598-021-83951-1)
29. Croci M, Vinje V, Rognes ME. 2019 Uncertainty quantification of parenchymal tracer distribution using random diffusion and convective velocity fields. *Fluids Barriers CNS* **16**, 32. (doi:10.1186/s12987-019-0152-7)
30. Poulain A, Riseth J, Vinje V. 2023 Multi-compartmental model of glymphatic clearance of solutes in brain tissue. *PLoS One* **18**, e0280501. (doi:10.1371/journal.pone.0280501)
31. Vinje V, Zapf B, Ringstad G, Eide PK, Rognes ME, Mardal KA. 2023 Human brain solute transport quantified by glymphatic MRI-informed biophysics during sleep and sleep deprivation. *Fluids Barriers CNS* **20**, 62. (doi:10.1186/s12987-023-00459-8)
32. Kress BT *et al*. 2014 Impairment of paravascular clearance pathways in the aging brain. *Ann. Neurol*. **76**, 845–861. (doi:10.1002/ana.24271)
33. Nedergaard M, Goldman SA. 2020 Glymphatic failure as a final common pathway to dementia. *Science* **370**, 50–56. (doi:10.1126/science.abb8739)
34. Peng W *et al*. 2016 Suppression of glymphatic fluid transport in a mouse model of Alzheimer's disease. *Neurobiol. Dis*. **93**, 215–225. (doi:10.1016/j.nbd.2016.05.015)
35. Xie L *et al*. 2013 Sleep drives metabolite clearance from the adult brain. *Science* **342**, 373–377. (doi:10.1126/science.1241224)
36. Holter KE *et al*. 2017 Interstitial solute transport in 3D reconstructed neuropil occurs by diffusion rather than bulk flow. *Proc. Natl Acad. Sci. USA* **114**, 9894–9899. (doi:10.1073/pnas.1706942114)
37. Nicholson C, Tao L. 1993 Hindered diffusion of high molecular weight compounds in brain extracellular microenvironment measured with integrative optical imaging. *Biophys. J*. **65**, 2277–2290. (doi:10.1016/S0006-3495(93)81324-9)
38. Kelley DH, Thomas JH. 2023 Cerebrospinal fluid flow. *Annu. Rev. Fluid Mech*. **55**, 237–264. (doi:10.1146/annurev-fluid-120720-011638)
39. Lee H, Mortensen K, Sanggaard S, Koch P, Brunner H, Quistorff B, Nedergaard M, Benveniste H. 2018 Quantitative gd-DOTA uptake from cerebrospinal fluid into rat brain using 3D VFA-SPGR at 9.4t. *Magn. Reson. Med*. **79**, 1568–1578. (doi:10.1002/mrm.26779)
40. Raicevic N, Forer JM, Ladrón-de-Guevara A, Du T, Nedergaard M, Kelley DH, Boster K. 2023 Sizes and shapes of perivascular spaces surrounding murine pial arteries. *Fluids Barriers CNS* **20**, 56. (doi:10.1186/s12987-023-00454-z)
41. Ray LA, Pike M, Simon M, Iliff JJ, Heys JJ. 2021 Quantitative analysis of macroscopic solute transport in the murine brain. *Fluids Barriers CNS* **18**, 55. (doi:10.1186/s12987-021-00290-z)
42. Basser PJ. 1992 Interstitial pressure, volume, and flow during infusion into brain tissue. *Microvasc. Res*. **44**, 143–165. (doi:10.1016/0026-2862(92)90077-3)
43. Asgari M, de Zélicourt D, Kurtcuoglu V. 2015 How astrocyte networks may contribute to cerebral metabolite clearance. *Sci. Rep*. **5**, 15024. (doi:10.1038/srep15024)
44. Katz MA, Barrette T, Krasovich M. 1992 Hydraulic conductivity of basement membrane with computed values for fiber radius and void volume ratio. *Am. J. Physiol. Heart Circ. Physiol*. **263**, H1417–H1421. (doi:10.1152/ajpheart.1992.263.5.H1417)
45. Yurchenco PD. 2011 Basement membranes: cell scaffoldings and signaling platforms. *Cold Spring Harb. Perspect. Biol*. **3**, a004911. (doi:10.1101/cshperspect.a004911)
46. Dreyer LW, Eklund A, Rognes ME, Malm J, Qvarlander S, Støverud KH, Mardal KA, Vinje V. 2024 Modeling CSF circulation and the glymphatic system during infusion using subject specific intracranial pressures and brain geometries. *bioRxiv*. (doi:10.1101/2024.04.08.588508)

47. Miyawaki T, Morikawa S, Susaki EA, Nakashima A, Takeuchi H, Yamaguchi S, Ueda HR, Ikegaya Y. 2020 Visualization and molecular characterization of whole-brain vascular networks with capillary resolution. *Nat. Commun*. **11**, 1104. (doi:10.1038/s41467-020-14786-z)
48. Mathiisen TM, Lehre KP, Danbolt NC, Ottersen OP. 2010 The perivascular astroglial sheath provides a complete covering of the brain microvessels: an electron microscopic 3D reconstruction. *Glia* **58**, 1094–1103. (doi:10.1002/glia.20990)
49. Korogod N, Petersen CCH, Knott GW. 2015 Ultrastructural analysis of adult mouse neocortex comparing aldehyde perfusion with cryo fixation. *eLife* **4**, e05793. (doi:10.7554/eLife.05793)
50. Blinder P, Shih AY, Rafie C, Kleinfeld D. 2010 Topological basis for the robust distribution of blood to rodent neocortex. *Proc. Natl Acad. Sci. USA* **107**, 12670–12675. (doi:10.1073/pnas.1007239107)
51. Adams MD, Winder AT, Blinder P, Drew PJ. 2018 The pial vasculature of the mouse develops according to a sensory-independent program. *Sci. Rep*. **8**, 9860. (doi:10.1038/s41598-018-27910-3)
52. Tithof J, Kelley DH, Mestre H, Nedergaard M, Thomas JH. 2019 Hydraulic resistance of periarterial spaces in the brain. *Fluids Barriers CNS* **16**, 19. (doi:10.1186/s12987-019-0140-y)
53. Hablitz LM, Plá V, Giannetto M, Vinitsky HS, Stæger FF, Metcalfe T, Nguyen R, Benrais A, Nedergaard M. 2020 Circadian control of brain glymphatic and lymphatic fluid flow. *Nat. Commun*. **11**, 4411. (doi:10.1038/s41467-020-18115-2)
54. Hablitz LM, Vinitsky HS, Sun Q, Stæger FF, Sigurdsson B, Mortensen KN, Lilius TO, Nedergaard M. 2019 Increased glymphatic influx is correlated with high EEG delta power and low heart rate in mice under anesthesia. *Sci. Adv*. **5**, eaav5447. (doi:10.1126/sciadv.aav5447)
55. Ray L, Iliff JJ, Heys JJ. 2019 Analysis of convective and diffusive transport in the brain interstitium. *Fluids Barriers CNS* **16**, 6. (doi:10.1186/s12987-019-0126-9)
56. Syková E, Nicholson C. 2008 Diffusion in brain extracellular space. *Physiol. Rev*. **88**, 1277–1340. (doi:10.1152/physrev.00027.2007)
57. Moses J, Sinclair B, Law M, O'Brien TJ, Vivash L. 2023 Automated methods for detecting and quantitation of enlarged perivascular spaces on MRI. *J. Magn. Reson. Imaging* **57**, 11–24. (doi:10.1002/jmri.28369)
58. Koch T, Vinje V, Mardal KA. 2023 Estimates of the permeability of extra-cellular pathways through the astrocyte endfoot sheath. *Fluids Barriers CNS* **20**, 20. (doi:10.1186/s12987-023-00421-8)
59. Bohr T *et al*. 2022 The glymphatic system: current understanding and modeling. *iScience* **25**, 104987. (doi:10.1016/j.isci.2022.104987)
60. Thomas JH. 2019 Fluid dynamics of cerebrospinal fluid flow in perivascular spaces. *J. R. Soc. Interface* **16**, 20190572. (doi:10.1098/rsif.2019.0572)
61. Faghih MM, Keith Sharp M. 2021 Mechanisms of tracer transport in cerebral perivascular spaces. *J. Biomech*. **118**, 110278. (doi:10.1016/j.jbiomech.2021.110278)
62. Schley D, Carare-Nnadi R, Please CP, Perry VH, Weller RO. 2006 Mechanisms to explain the reverse perivascular transport of solutes out of the brain. *J. Theor. Biol*. **238**, 962–974. (doi:10.1016/j.jtbi.2005.07.005)
63. Kedarasetti RT, Turner KL, Echagarruga C, Gluckman BJ, Drew PJ, Costanzo F. 2020 Functional hyperemia drives fluid exchange in the paravascular space. *Fluids Barriers CNS* **17**, 52. (doi:10.1186/s12987-020-00214-3)
64. Mestre H *et al*. 2020 Cerebrospinal fluid influx drives acute ischemic tissue swelling. *Science* **367**, eaax7171–24. (doi:10.1126/science.aax7171)
65. Du T *et al*. 2022 Cerebrospinal fluid is a significant fluid source for anoxic cerebral oedema. *Brain* **145**, 787–797. (doi:10.1093/brain/awab293)
66. Quirk K. 2024 Network model of solute transport (1.0). *Zenodo.* (doi:10.5281/zenodo.11385333)